Supplementary Material to "Sensing coherent dynamics of electronic spin clusters in solids"

E. L. Rosenfeld[1], L. M. Pham[2], M. D. Lukin[1], R. L. Walsworth[1,3]
[1]Department of Physics, Harvard University, Cambridge, Massachusetts 02138, USA
[2]MIT Lincoln Laboratory, Lexington Massachusetts 02139, USA
[3]Harvard-Smithsonian Center for Astrophysics, Cambridge, Massachusetts 02138, USA

June 8, 2018

1 Experimental setup

1.1 Optical setup

We use a home-built 4f confocal microscope to initialize and read out the NV photoluminescence, and a 532 nm green diode laser (Changchun New Industries Optoelectronics Tech Co, Ltd, MGL H532), for NV illumination and initialization. The laser pulses are modulated using an acousto-optic modulator (IntraAction ATM series 125B1), which is gated using a pulseblaster card (PulseBlasterESR-Pro, SpinCore Technologies, Inc, 300 MHz). We use an initialization pulse duration of 3.8 μs, of which 880 ns is used for readout of the NV ground state. The NV fluorescence is filtered using a dichroic mirror (Semrock FF560-FDi01) and notch filter (Thorlabs FL-532), and read out using a single photon counter (Excelitas Technologies, SPCM-AQRH-13-FC 17910). A galvonometer (Thorlabs GVS002) scans the laser in the transverse plane, and a piezoelectric scanner placed underneath the objective (oil immersion, Nikon N100X-PFO, NA of 1.3) is used to focus. The diamond is mounted on a glass coverslip patterned with a stripline for microwave delivery (see section 1.2), which is placed directly above the oil immersion objective lens.

1.2 Microwave driving of the NV and electron spins

A dual-channel arbitrary waveform generator (Tektronix AWG7102) is used to synthesize the waveforms for the NV and electron spin drives for all pulse sequences. The AWG output is triggered using the pulseblaster card. The NV drive and electron spin drives are amplified separately (Minicircuits ZHL-42W+, Minicircuits ZHL-16W-43-S+, respectively), then combined using a high power combiner (Minicircuits ZACS242-100W+). The microwave signals are then connected to an Ω-shaped stripline, 100 μm inner diameter, via a printed circuit board. The diamond is placed onto the center Ω of the stripline. Typical Rabi frequencies for the NV and electron spins (around 900 and 2000 MHz, respectively) are between 10-15 MHz.

1.3 Diamond sample

The diamond substrate was grown by chemical vapor deposition at Element Six, LTD. It is a polycrystalline, electronic grade substrate. A 99.999% 12-C layer was grown on the substrate, also at Element Six, along the {110} direction, and the diamond was left unpolished. Implantation was performed at Ruhr Universität in Bochum, Germany. Both atomic and molecular ions, ^{14}N and $^{14}N_2$, were implanted separately, in a mask pattern with confined circles approximately 30 μm in diameter, at 2.5 keV implantation energy. The density of implantation varies from 1.4x10^{12}/cm^2 to 1.4x10^9/cm^2 in different mask regions. For the present study, an NV found near the 1.4x10^{12}/cm^2 ion implant region is used. The sample was annealed in vacuum at 900°C for 8 hours.

About 400-500 NVs were investigated, and over 75% were found to have poor contrast or the incorrect orientation in the bias field. Of the total number of NVs investigated, 113 NVs were screened for coupling to dark spins. The NVs are implanted to be about 5-10 nm below the surface, such that there is a high probability to detect surface dark spins (we expect from e.g.

dangling bonds close to the diamond edge). Of the 113 NVs screened for dark spin coupling, about 9 demonstrated coherent coupling to dark spin(s), 63 demonstrated incoherent coupling to a bath of dark spins, and 41 exhibited no signature of dark spin coupling. The individual NV described in our manuscript had coherent coupling to multiple dark spins, and was also very stable in its behavior (for more than a year while the experiments were performed). A frontier challenge in the NV-diamond community is to fabricate, reliably and predictably, NVs and dark spins with coherent couplings and other optimal properties, so that such mass screenings are not necessary.

1.4 Static bias field

We use a permanent magnet (K&J Magnetics, Inc, DX08BR-N52) to induce a magnetic field B_0 and thereby split the NV and electron spin energy levels. The diamond is mounted on a three-axis translation stage, which is controlled by three motorized actuators (Thorlabs Z812B). To align the magnetic field to the NV axis, we sweep the position of the magnet, monitor the NV fluorescence (which decreases with field misalignment due to mixing of the magnetic sublevels) and fix the magnet position to the point of maximum count rate. Field alignment precision is about 2°, given by the shot noise of our fluorescence measurements. In order to stabilize the magnitude of the B_0 field at our system during an experiment, we periodically (approximately every 15 minutes) measure the $m_s = 0 \rightarrow -1$ transition frequency of the NV, and move the magnet position to stabilize the NV transition frequency, and therefore field, at a particular value. Using this technique, we can stabilize the field enough to resolve the ∼1 MHz splittings in the DEER ESR experiment, despite the 0.1%/K temperature coefficient of Neodymium magnets [2]. Our B_0 measurement is taken from the NV transition frequency, which therefore includes error from the 2° field misalignment, as well as the approximate error of a measurement of this particular NV zero field splitting, of 2.872(2) GHz, to give a B_0 measurement accuracy of about 0.1%.

2 Signal frequencies and amplitudes in the SEDOR experiment

In this section we discuss the frequencies seen in the SEDOR experiment, referring to Figs. 3(b) and 3(c) in the main text.

As stated in the main text, the Hamiltonian is:

$$\frac{\mathcal{H}}{h} = \sum_{i=1,2} \Big(\omega_i + A_i\Big(S_z^{\mathrm{NV}} + \mathbf{I}/2\Big)\Big) S_z^{(i)} + \tag{1}$$

$$J_{12}\Big(2S_z^{(1)}S_z^{(2)} - \frac{1}{2}(S_+^{(1)}S_-^{(2)} + S_-^{(1)}S_+^{(2)})\Big) \tag{2}$$

Where $\omega_1 = \gamma_e B_0 + 0(2)$ MHz, $\omega_2 = \omega_1 - 0.14(5)$ MHz, are the resonance frequencies electron spins 1 and 2, $A_{1,2} = 0.81(5), -0.86(5)$ MHz, are the negative of their couplings to the NV, and $J_{12} = \pm 0.38(5)$ MHz is half the electron spin – spin coupling.

The states of the electron spins $|\uparrow\uparrow\rangle$ and $|\downarrow\downarrow\rangle$ are decoupled from the states $|\uparrow\downarrow\rangle$ and $|\downarrow\uparrow\rangle$, because the Hamiltonian and SEDOR pulse sequence conserve $|S_z^{(1)} + S_z^{(2)}|$. Therefore, we consider those two subspaces separately.

For the electron spin states $|\uparrow\uparrow\rangle$ and $|\downarrow\downarrow\rangle$ the flip-flop terms are zero, and the Ising interaction term $S_z^{(1)}S_z^{(2)}$ is a constant, so the only relevant terms are:

$$\frac{\mathcal{H}}{h} = \sum_{i=1,2} \Big(\omega_i + A_i\Big(S_z^{\mathrm{NV}} + \mathbf{I}/2\Big)\Big) S_z^{(i)}. \tag{3}$$

The NV accumulates phase due to its the secular dipolar coupling to the electron spins. Therefore, the NV signal rotates at $\Delta_4/2 = (A_1 + A_2)/2$ before phase modulation.

For the $|\uparrow\downarrow\rangle$ and $|\downarrow\uparrow\rangle$ states, we need to consider the dynamics. Treating this subspace as a two level system where $|\Uparrow\rangle = |\uparrow\downarrow\rangle$ and $|\Downarrow\rangle = |\downarrow\uparrow\rangle$ and dropping the Ising interaction term, we have:

$$\frac{\mathcal{H}}{h} = \Big(\delta + a(S_z^{\mathrm{NV}} + \mathbf{I}/2)\Big) s_z + J_{12} s_x. \tag{4}$$

Table 2.1: Frequency components in the SEDOR experiment and their values. The frequency name Δ_i and the form calculated using equation (1) in the main text and the SEDOR pulse sequence are listed as 'Frequency' and 'Form'. The frequency values in our model, in MHz, from the calculation are listed as 'Model (MHz)'. The frequency values extracted from the fit of the time-domain SEDOR data shown in Figure 3(b) are listed as 'Fit (3(b)) (MHz)'. Error bars are 95% CI. For intuition, the states responsible for each frequency component in the SEDOR data are listed as 'Relevant states'. Frequency Δ_1 is the dark spin flip-flop rate, corresponding to $|0\rangle_{\mathrm{NV}}$; frequency Δ_2 results from the dipolar magnetic field generated by the dark spins in the $|\uparrow\downarrow\rangle$, $|\downarrow\uparrow\rangle$ subspace, while flip-flops are suppressed by the NV field gradient generated by $|-1\rangle_{\mathrm{NV}}$; frequency Δ_3 is due to the interference of the two paths generated by the NV coherence; and frequency Δ_4 results from the field generated by the dark spins at the NV from the $|\uparrow\uparrow\rangle$, $|\downarrow\downarrow\rangle$ subspace. It is indistinguishable from the component at DC generated by the electron spin dynamics.

Frequency	Form	Model (MHz)	Fit (3(b)) (MHz)	Relevant states
Δ_1	$\sqrt{J_{12}^2+(\omega_1-\omega_2)^2}$	0.41(5)	0.391(8)	$\|0\rangle_{\mathrm{NV}}\otimes(\|\uparrow\downarrow\rangle,\|\downarrow\uparrow\rangle)$
Δ_2	$\sqrt{(A_1-A_2+\omega_1-\omega_2)^2+J_{12}^2}$	1.85(8)	1.790(9)	$\|-1\rangle_{\mathrm{NV}}\otimes(\|\uparrow\downarrow\rangle,\|\downarrow\uparrow\rangle)$
Δ_3	$\sqrt{(A_1-A_2+\omega_1-\omega_2)^2+J_{12}^2}-\sqrt{J_{12}^2+(\omega_1-\omega_2)^2}$	1.44(4)	1.430(7)	$\|0,-1\rangle_{\mathrm{NV}}\otimes(\|\uparrow\downarrow\rangle,\|\downarrow\uparrow\rangle)$
Δ_4	A_1+A_2	−0.05(7)	0.00(7)	$\|0,-1\rangle_{\mathrm{NV}}\otimes(\|\downarrow\downarrow\rangle,\|\uparrow\uparrow\rangle)$

Where $\delta=\omega_1-\omega_2$ and $a=A_1-A_2$. We use s_i to represent the new $\mathrm{S}=1/2$ spin operators. Here we define two Hamiltonians: one for the NV population in $m_s=0$, defined as $\mathcal{H}_0/h=\delta s_z+J_{12}s_x$, and conversely one for the NV population in $m_s=-1$, defined as $\mathcal{H}_{-1}/h=(\delta+a)s_z+J_{12}s_x$. We use the operators $s_{x,y,z}$ to denote the new electron spin operators in the new 2x2 subspace. Let the unitaries $U_{0,-1}(t)\equiv e^{-i\mathcal{H}_{0,-1}t/\hbar}$.

At the start of the pulse sequence, with the NV starting in $|-1\rangle_{\mathrm{NV}}$, and immediately following the first $\pi/2$ pulse on the NV about y, the density matrix is:

$$\rho(0)=(|0\rangle\langle 0|+|0\rangle\langle -1|+|-1\rangle\langle 0|+|-1\rangle\langle -1|)\otimes\mathbf{I}/2. \tag{5}$$

After the SEDOR sequence with free precession time τ, the density matrix is:

$$\rho(0)=|0\rangle\langle 0|+ \tag{6}$$
$$U_{-1}(\tau/2)\sigma_x U_0(\tau/2)\,|0\rangle\langle -1|\,U_{-1}(\tau/2)^\dagger\sigma_x U_0(\tau/2)^\dagger+ \tag{7}$$
$$U_0(\tau/2)\sigma_x U_{-1}(\tau/2)\,|-1\rangle\langle 0|\,U_0(\tau/2)^\dagger\sigma_x U_{-1}(\tau/2)^\dagger+ \tag{8}$$
$$|-1\rangle\langle -1|\,. \tag{9}$$

Where for each term there is an implicit $\mathbf{I}/2$ for the electron spin subspace $|\Uparrow\rangle$ and $|\Downarrow\rangle$. As expected, the population terms stay the same and the coherence terms accumulate phase. Tracing over the electron spins' subspace, our signal is therefore given by $\mathrm{Tr}(S_x^{\mathrm{NV}}\rho)$, which is proportional to the trace of the matrix $(U_{-1}(\tau/2)\sigma_x U_0(\tau/2))^\dagger U_0(\tau/2)\sigma_x U_{-1}(\tau/2)$.

The frequency components in this part of the signal are $\Delta_1/2=\frac{1}{2}\sqrt{J_{12}^2+\delta^2}$, $\Delta_2/2=\frac{1}{2}\sqrt{J_{12}^2+(A_1-A_2+\delta)^2}$, and $\Delta_3/2=(\Delta_2-\Delta_1)/2$, as expected. There is also a frequency component at DC, in addition to the component at $(A_1+A_2)/2$ mentioned above. We do not include this component in our analysis, since it is indistinguishable from $(A_1+A_2)/2$.

2.1 Phase modulation

By sweeping the phase ϕ of the last $\pi/2$ pulse, such that $\phi=2\pi\nu\tau$, any signal component proportional to $\cos(2\pi(\Delta_i\tau/2))$ will be converted to $\cos(2\pi(\Delta_i/2+\nu)\tau)+\cos(2\pi(\Delta_i/2-\nu)\tau)$. These positive and negative frequency components correspond to the polarization of the electron spins. For example, if at the start of the sequence the electrons' spin states begin in the state $|\uparrow\downarrow\rangle$, the NV Bloch vector will rotate clockwise in the transverse plane, with rate 0.84(5) MHz. Conversely, if the electrons' spin states start in the state $|\downarrow\uparrow\rangle$, the NV Bloch vector will rotate counter-clockwise at the same rate. After the last $\pi/2$ pulse, which is responsible for the frequency up-conversion, the corresponding signal frequency is (0.84(5) $\pm\nu$) MHz, respectively.

Frequency	Amplitude Form	Relative Amplitude
$\Delta_1/2$	$\frac{1}{\Delta_1^2\Delta_2^2}\left(\Delta_2^2(J_{12}^2-\delta^2)-\Gamma+\Delta_1^2(J_{12}^2-\delta_1^2)+\Delta_1^2\Delta_2^2\right)$	1.00
$\Delta_2/2$	same as Δ_1	1.00
$\Delta_3/2$	$\frac{1}{2\Delta_1^2\Delta_2^2}\left(\Delta_2^2(\delta^2-J_{12}^2)+\Gamma+\Delta_1^2\Delta_2^2+\Delta_1^2(\delta_1^2-J_{12}^2)+4\delta\delta_1\Delta_1\Delta_2\right)$	1.05
$(\Delta_1+\Delta_2)/2$	$\frac{1}{2\Delta_1^2\Delta_2^2}\left(\Delta_2^2(\delta^2-J_{12}^2)+\Gamma+\Delta_1^2\Delta_2^2+\Delta_1^2(\delta_1^2-J_{12}^2)-4\delta\delta_1\Delta_1\Delta_2\right)$	0.21
DC	$\frac{1}{\Delta_1^2\Delta_2^2}\left(\Delta_2^2(\delta^2-J_{12}^2)+\Gamma+\Delta_1^2\Delta_2^2+\Delta_1^2(-\delta_1^2+J_{12}^2)\right)$	1.10

Table 2.2: SEDOR frequencies and their relative amplitudes, normalized to the $\Delta_1/2$ frequency component. Here, $\delta \equiv \omega_1 - \omega_2 = 0.14$ MHz is the energy difference between the dark spin states $|{\downarrow\uparrow}\rangle$ and $|{\uparrow\downarrow}\rangle$, when the NV population is in $m_s = 0$, $\delta_1 \equiv A_1 - A_2 + \delta = 1.81$ MHz is the energy difference between the dark spin states $|{\downarrow\uparrow}\rangle$ and $|{\uparrow\downarrow}\rangle$, when the NV population is in $m_s = -1$, and $\Gamma \equiv \delta^2\delta_1^2 + \delta^2 J_{12}^2 + \delta_1^2 J_{12}^2 + J_{12}^4$. Note that the $(\Delta_1+\Delta_2)/2$ component is suppressed (given by the sign of δ). The amplitudes in Figures 3(c) and 4(b) agree with these values within the experimental noise floor.

3 Parameter values and error ranges

The frequency values from the time-domain fit in Figure 3(b) of the main text, as well as the model frequency values, are reported in Table 2.1. For $\Delta_{1,2,3}$, the frequency values are extracted from a fit of the absolute value of the FFT of the SEDOR data in Figure 3(b) of the main text, to a sum of three Lorentzian lineshapes. We use a fit in the absolute value of the frequency domain, as opposed to the time domain, in order to inform our $\Delta_{1,2,3}$ frequencies with fewer fit parameters (the phases in the time domain data are sensitive to pulse errors and are therefore free parameters). Although the fits in the frequency and time domain agree within the error ranges [Table 2.1], we expect small differences occur because of our approximation of the frequency domain lineshape as Lorentzian. As listed in Table 2.1 and stated in the main text, we find frequency values for $\Delta_{1,2,3}$ of 0.41(5), 1.85(8), and 1.44(4) MHz, respectively. We use frequencies $\Delta_{1,2,3}$ to extract the parameter values J_{12}, $A_1 - A_2$, and $\omega_1 - \omega_2$, as well as the lower bound on $|A_1 + A_2|$ of 50 kHz. Due to the existence of multiple solutions to this system of equations, we impose agreement to the splitting in the NV ESR spectrum and the value of $A_1 - A_2$ to find our parameter values. The frequency of oscillation in our Hartmann-Hahn experiments [Fig. 4(a) in the main text] confirms our result. Finally, we check for qualitative agreement between the DEER ESR spectrum and a numerical simulation of our model and the DEER ESR pulse sequence. As mentioned in the main text, the DEER ESR lineshape is very sensitive to all parameter values [Fig. 3.2]. This allows for finding the value of $A_1 + A_2$ within the lower bound found from the SEDOR experiment and hence A_1 and A_2. Additionally, the value of ω_1, and therefore $\omega_2 = \omega_1 - 0.14(5)$ MHz, can be found by centering the central DEER ESR dip with the dip found numerically. We find that ω_1 is indistinguishable from the bare electron Zeeman splitting at $g = 2$ (within the experimental error, see below). We note that the exact values of $A_1 + A_2$ and ω_1 are irrelavant to our observation of coherent dynamics, since $A_1 + A_2$ is unresolved in the SEDOR experiment, and the Hamiltonian conserves $|S_z^{(1)} + S_z^{(2)}|$, such that the common-mode Zeeman energy splitting of both spins is inconsequential.

To account for the finite spectral resolution shifting our fit frequency, we add an uncertainty of half of the spectral resolution (approximating this to be the 95% CI) to the error in the frequency-domain fit. We expect that the small differences between the frequencies extracted from the time domain fit and the frequency domain fit, which are within the experimental uncertainty, are due to approximating the frequency-domain lineshapes as Lorentzians. The error of the Δ_4 frequency is calculated using the estimated error ranges on our parameter values of 50 kHz. The amplitude of a fourth frequency component, $(\Delta_2 + \Delta_1)/2$, is suppressed for our parameters, as shown in Table 2.2.

According to our model, the frequencies that appear in the SEDOR experiment are various combinations of the parameters added in quadrature, which we use to inform the coupling strengths reported. These measurements have finite widths and degrees of reproducibility, as seen in Figs.

3(b) and 3(c) in the main text. We expect that the variability of our measurements is due to B_0 field misalignment changing the secular coupling strengths and drive amplitude instability inducing pulse errors during our characterization experiments. In this section, we describe the procedure used to obtain the model parameter error ranges reported in the main text.

We measure the degree of reproducibility of the SEDOR experiment by repeating the experiment six times over the course of our data-taking period (about 6 months). To extract the SEDOR frequencies $\Delta_{1,2,3}$, we fit the Fourier transform of the SEDOR data to a sum of three Lorentzian curves, and extract the center frequency as well as 95% CI on the fit (to account for photon shot noise). Due to the finite spectral resolution of our experiment, which is on the order of the widths that we measure, we add a contribution to the error equal to half the frequency spacing in our SEDOR experiments (approximating 95% CI to be the full frequency spacing). The SEDOR frequencies obtained for the six measurements, with the error ranges found, are plotted in Figure 3.1. For each of the SEDOR frequencies $\Delta_{1,2,3}$, we define the range of the frequency value to be $\max(\Delta_i) + \sigma_{\max(\Delta_i)} - (\min(\Delta_i) + \sigma_{\min(\Delta_i)})$, where σ is defined to be the 95% CI for the relevant measurement.

Given the form for Δ_{1-3} reported in the main text, we estimate the drift and error range for each of the parameter values, by taking the average of the ranges of the $\Delta_{1,2}$ values, divided by $2\sqrt{2}$, or approximately 50 kHz.

The error in ω_1, and consequently the common mode error in $\omega_2 = -0.14$ MHz $+ \omega_1$ is given by the B_0 field misalignment which, as mentioned in Section 1.4 is about 2°. At 694.0 G, this is about 0.5 G or 1.4 MHz. A measurement of our NV's zero field splitting gives a value of 2.7817 $\pm$0.0015 GHz, adding to the B_0 uncertainty. The ω_1 value is about $\gamma_e B_0 + 0^{+1.5}_{-2.0}$ MHz. We find that the DEER ESR lineshape qualitative agreement occurs within this window around the bare electron Zeeman splitting.

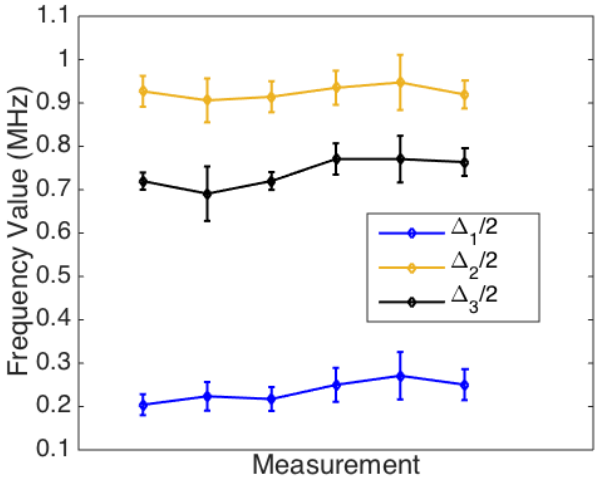

Figure 3.1: SEDOR frequency values $\Delta_{1,2,3}/2$ measured over the data-taking period. Values are extracted from a fit to the FFT of the SEDOR data using a sum of three Lorentzian lineshapes. Error bars account for the 95% CI of the fit as well as the finite spectral resolution shifting the fit frequency (approximating full-width 95% CI as the spectral resolution).

3.1 Comparison of DEER ESR spectra for various coupling strength values

In this section, we demonstrate the qualitative agreement between our DEER ESR spectrum and our model, within the error range on the parameters reported. As in the main text, we simulate the results of the DEER ESR experiment by numerically calculating the ODMR lineshape under the DEER ESR pulse sequence, for our spin cluster Hamiltonian and parameters. To explore the sensitivity of our lineshape to our parameter values, we repeat the numerical calculation, changing the parameter values one at a time, and compare the results to the same data. Figure 3.2

Figure 3.2: DEER ESR lineshapes calculated numerically using parameter values within the error range reported in the main text. Black circles are data, and red line is the DEER ESR lineshape calculated numerically for the parameter values given in the main text. Blue lines are DEER ESR results calculated numerically for parameter values listed.

(a) Blue line: DEER ESR lineshape calculated numerically, using parameter values listed in the main text, except with $J_{12} = 0.43$ MHz, or 50 kHz more than the J_{12} reported.

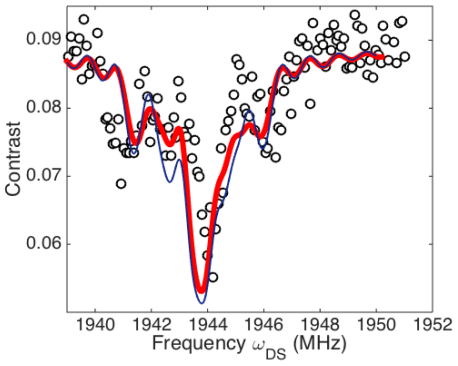

(b) Blue line: DEER ESR lineshape calculated numerically, using parameter values listed in the main text, except with $J_{12} = 0.33$ MHz, or 50 kHz less than the J_{12} reported.

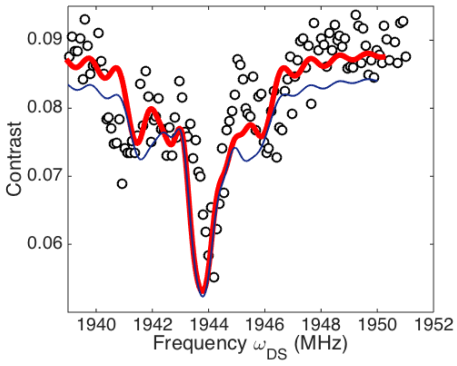

(c) Blue line: DEER ESR lineshape calculated numerically, using parameter values listed in the main text, except with $A_1 = 0.86$ MHz, or 50 kHz greater than the A_1 reported.

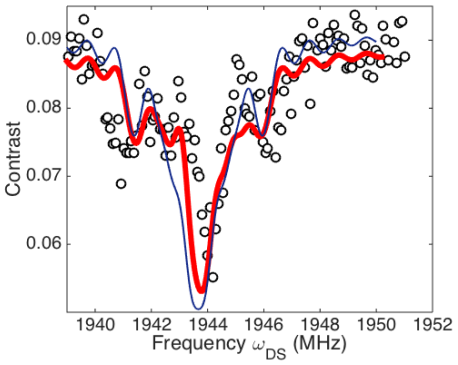

(d) Blue line: DEER ESR lineshape calculated numerically, using parameter values listed in the main text, except with $A_2 = -0.76$ MHz, or 100 kHz less negative than the A_2 reported, beyond the error range in our parameters.

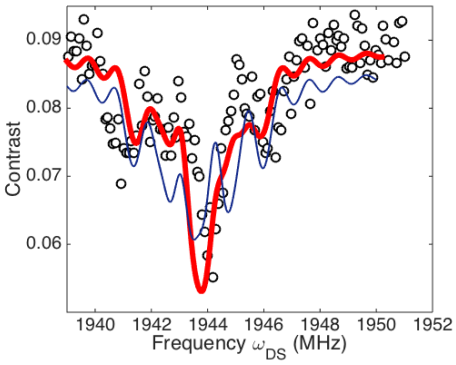

demonstrates qualitative agreement between the DEER ESR data and our model for parameter values within the error range reported in the main text. For parameter values simulated beyond the error range, as in Figure 3.2(d), the numerically calculated DEER ESR lineshape clearly disagrees with the DEER ESR data obtained. Changing the relative detuning $\omega_1 - \omega_2$ between the electron spins and the other coupling strength A_1, at and beyond the error bar ranges, gives similar qualitative results.

4 SEDOR frequency component at the phase cycling frequency due to pulse errors

In this section we characterize the amplitude of the NV-electron spin SEDOR signal at the phase modulation frequency, ν, when there are imperfect pulses. Although there is a component of the SEDOR signal predicted to be at ν, the amplitude can depend on pulse errors, as calculated below. The SEDOR pulse sequence is illustrated in Figure 3(a) in the main text. The intuitive idea is that if, due to detuned driving, the electron spin is not fully flipped, then there is some component of NV coherence that is left oscillating purely at the phase modulation frequency. Here we calculate the amplitude of that component as a function of the Rabi frequency and detuning.

In this section we evaluate the density matrix at various points in the evolution of the sequence, instead of multiplying unitaries and taking a trace at the end, in order to account for the finite electron spin coherence time.

4.1 Hamiltonian and pulse sequence

To gain a qualitative understanding of the component at ν due to pulse errors, we imagine an NV (NV) and single electronic dark spin (DS) system. We assume that their resonance frequencies are detuned from each other much more than both their linewidths and coupling strength $A_{||}$. Additionally, we incorporate an RF drive on the NV and dark spin, and we assume that the drive on the NV is resonant (we are ignoring NV hyperfine splitting), and that the dark spin drive is detuned by δ. Treating the NV in a 2x2 subspace, we absorb the extra $A_{||}/2S_z^{\mathrm{DS}}$ term (the third term in equation (1) in the main text) into δ:

$$H = A_{||} S_z^{\mathrm{NV}} S_z^{\mathrm{DS}} + H_{RF}(t). \tag{10}$$

The pulse sequence is a Hahn echo on the NV, with the NV π pulse coincident with a dark spin detuned π pulse. The full free precession time is 2t. We assume perfect pulses on the NV, and a π pulse of duration T on the dark spin. The goal is to see if there is any component of the NV coherence at the end of the pulse sequence that does not oscillate, i.e., a component that will be upconverted to ν after adding phase modulation.

4.2 Dynamics

We start with a polarized state on the NV, $S_z^{\mathrm{NV}} + \mathbf{I}^{\mathrm{NV}}/2$ and a fully mixed state on the dark spin, $\mathbf{I}^{\mathrm{DS}}/2$. After the first $\pi/2$ pulse on the NV, along y, the density matrix is then

$$\rho = (S_x^{\mathrm{NV}} + \mathbf{I}^{\mathrm{NV}}/2)) \otimes \mathbf{I}/2. \tag{11}$$

(We use the notation $S_x \equiv S_x \otimes \mathbf{I}/2$ here for simplicity.)

After the first part of the free evolution time we have:

$$\rho(t) = S_x^{\mathrm{NV}} \cos A_{||} t/2 + 2 S_y^{\mathrm{NV}} S_z^{\mathrm{DS}} \sin A_{||} t/2. \tag{12}$$

Next we have a π pulse on both the NV (about x) and the dark spin (about x), with the dark spin pulse detuned by δ and for duration $T << 1/A_{||}$, such that $H_{eff}^{\mathrm{DS}} = \delta S_z^{\mathrm{DS}} + \Omega_{\mathrm{DS}} S_x^{\mathrm{DS}}$. We assume also that the difference in the NV and dark spin resonance frequencies (order 1 GHz) is much greater than either Rabi frequency.

$$\rho(t+T) = S_x^{\mathrm{NV}} \cos A_{||} t/2 \tag{13}$$

$$-2 S_y^{\mathrm{NV}} \sin A_{||} t/2 \left(e^{-i(\delta S_z^{\mathrm{DS}} + \Omega_{\mathrm{DS}} S_x^{\mathrm{DS}})T} \right) S_z^{\mathrm{DS}} \left(e^{i(\delta S_z^{\mathrm{DS}} + \Omega_{\mathrm{DS}} S_x^{\mathrm{DS}})T} \right) \tag{14}$$

To solve for the dark spin dynamics under the detuned pulse we need to go into a tilted frame to diagonalize the dark spin Hamiltonian. Choosing $U = e^{-i\theta S_y^{\mathrm{DS}}}$ we have $H_{eff}^{\mathrm{DS}} = \bar{\Omega}_{\mathrm{DS}} S_z^{\mathrm{DS}}$ where $\bar{\Omega}_{\mathrm{DS}} = \sqrt{\Omega_{\mathrm{DS}}^2 + \delta^2}$ and $\theta = \arctan -\Omega_{\mathrm{DS}}/\delta$. After going into the tilted frame and applying the detuned pulse, we account for evolution during the second half of the free precession time. After transforming back into the un-tilted frame, we drop all $S_{x,y}^{\mathrm{DS}}$ terms, since the dark spin $T_2^* << 1/A_{||}$. Allowing for the second half of the free precession time, we find a final density matrix of:

$$\rho(2t+T) = S_x^{\mathrm{NV}} \cos^2 A_{||} t/2 + 2 S_y^{\mathrm{NV}} S_z^{\mathrm{DS}} \cos A_{||} t/2 \sin A_{||} t/2 \tag{15}$$

$$- \cos^2\theta \sin A_{||} t/2 \Big(2 S_y^{\mathrm{NV}} S_z^{\mathrm{DS}} \cos A_{||} t/2 - S_x^{\mathrm{NV}} \sin A_{||} t/2 \Big) \tag{16}$$

$$- \cos \bar{\Omega}_{\mathrm{DS}} T \sin^2\theta \sin A_{||} t/2 \Big(2 S_y^{\mathrm{NV}} S_z^{\mathrm{DS}} \cos A_{||} t/2 - S_x^{\mathrm{NV}} \sin A_{||} t/2 \Big) \tag{17}$$

Since the dark spin is unpolarized, any term that evolves as S_z^{DS} will add a mixed state contribution and therefore not contribute to any NV coherence oscillation. So the "signal" terms are:

$$\rho(2t+T) \sim S_x (\cos^2 A_{||} t/2 + \cos^2\theta \sin^2 A_{||} t/2 + \cos \bar{\Omega} T \sin^2\theta \sin^2 A_{||} t/2). \tag{18}$$

As a check, if we have $\bar{\Omega} T = \pi$ and $\delta = 0$ meaning $\theta = \pi/2$, we would find $\rho(2t+T) \sim S_x(\cos^2 A_{||} t/2 - \sin^2 A_{||} t/2) = S_x(\cos A_{||} t)$ as desired.

4.3 Results

For $\delta \neq 0$, we set $\bar{\Omega}_{\mathrm{DS}} T = \pi$ and calculate the resulting NV coherence:

$$\rho(2t+T) \sim S_x(\cos^2 A_{||} t/2 + \sin^2 A_{||} t/2 (\cos^2\theta - \sin^2\theta) \tag{19}$$

$$= S_x(\cos^2\theta + \sin^2\theta \cos A_{||} t) \tag{20}$$

Clearly there is a component that does not oscillate, i.e., the $\cos^2\theta$ component. After applying the last $\pi/2$ pulse and phase modulation, this component will oscillate purely at the phase modulation frequency. This component at DC has an amplitude of $\cos^2\theta = \delta^2/(\Omega_{\mathrm{DS}}^2 + \delta^2)$. If $\bar{\Omega}_{\mathrm{DS}} T = (2n+1)\pi/2$, we are left with:

$$\rho(2t+T) \sim S_x(\cos^2 A_{||} t/2 + \cos^2\theta \sin^2 A_{||} t/2) \tag{21}$$

$$= S_x(\cos^2\theta + (1/2)\sin^2\theta - \sin^2\theta \cos A_{||} t) \tag{22}$$

In this case we find a component proportional to $(\delta^2 + (1/2)\Omega_{\mathrm{DS}}^2)/(\delta^2 + \Omega_{\mathrm{DS}}^2)$ which is always significant.

As desired, the only case where most of the population is actually oscillating at the dipole coupling strength $A_{||}$ is when $\delta/\Omega_{\mathrm{DS}} << 1$ and $\bar{\Omega}_{\mathrm{DS}} T = n\pi$ with n odd.

In our experiment, δ is of order 1 MHz and Ω is of order 13 MHz. For a π pulse, the extra amplitude component in ν is approximately $\cos^2\theta$, which for these parameters is about 0.6%.

5 S quantum number of the electron spins

The electron spins are determined to be S = 1/2 by comparing the measured NV Rabi frequency, Ω_{NV}, to the electron spin Rabi frequency, Ω_{DS}, for known resonant drive field amplitudes. The NV spin transitions are properly treated in a 2x2 subspace, although the NV electronic spin has S = 1, because the other NV spin transition is far off resonance for our experimental conditions. Thus, the normalized magnitude of the NV $S_{x,y}$ matrix elements are $1/\sqrt{2}$. For S = 1/2, the normalized magnitude of the $S_{x,y}$ matrix elements are 1/2. From our experiments we find $\Omega_{\mathrm{NV}}/\Omega_{\mathrm{DS}} = \sqrt{2}$, as expected for S = 1/2 electron spins. This technique for spin quantum number identification is commonly used in EPR [1].

We are careful to use the same electronics and carrier frequency for both measurements, by tuning the B_0 field between measurements such that the resonance frequency of the NV $m_s = 0 \rightarrow m_s = -1$ transition during the Ω_{NV} measurement is equal to the electron spin resonance frequency during the Ω_{DS} measurement. In this case, the resonance frequency of both spins was 927.2 MHz.

Running a Rabi experiment on the NV, we see coherent oscillations [Fig. 5.1]. The Rabi frequency extracted from fitting the data is 18.5(2) MHz.

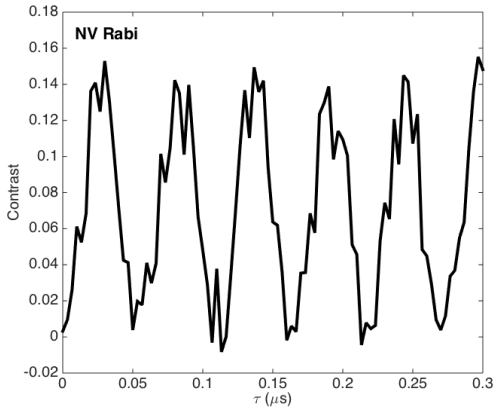

Figure 5.1: Rabi flopping of the NV, at a resonance frequency of 927.2 MHz. Here, τ is the NV pulse duration, the Y axis is contrast. A sinusoidal fit to the data gives a Rabi frequency of 18.5(2) MHz.

We immediately perform a DEER Rabi pulse sequence to extract the Rabi frequency of the electron spins, with the field B_0 set such that the resonance frequency of the electron spins is at about 927 MHz, to avoid frequency-dependent power delivery of the setup affecting our S value measurement. We see multiple frequency components in the resulting FFT [Fig. 5.2] of the time-domain data, due to the fact that the coupling time τ is longer than the interaction period $1/A_1 \approx 1/A_2$. We find a primary frequency of 13.3(1) MHz, with the harmonics from this feature appearing in the spectrum. Since $\Omega_{\mathrm{NV}}/\Omega_{\mathrm{DS}} = \sqrt{2}$ within their error bars, we conclude that both electron spins are S = 1/2.

These measurements show that the dark spins are S = 1/2 electronic spins with no nuclear spins present. To our knowledge, the only possibility in diamond for stable S = 1/2 electronic defects with no nuclear spins is the V+ defect.

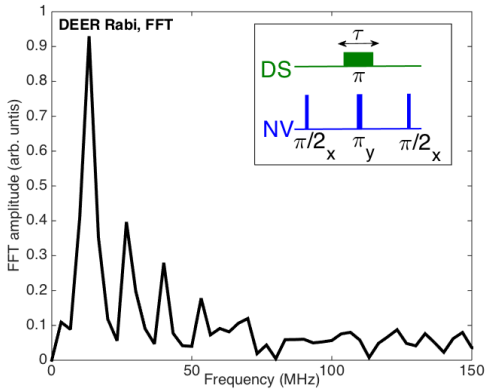

Figure 5.2: FFT of the DEER Rabi experiment on the electron spins, at a spin resonance frequency of 927.2 MHz. The primary frequency of 13.3 MHz corresponds to the electron spin Rabi frequency, and the harmonics are from pulse errors in the sequence due to the long NV-electron spin coupling time.

6 Zeeman spectroscopy of the electron spins

The electron spins' resonance frequencies closely follow the bare electron $g = 2$ value in our experiment. In general, the order of magnitude $\sim 10^{-4}$ shift from $g = 2$ that we find is consistent with other g anisotropy values for other S = 1/2 defects in diamond [3, 4, 5]. To demonstrate their bare electron character, we perform Zeeman spectroscopy by changing the value of the B_0 field and measuring the transition frequencies. We move a permanent magnet nearby and align it to the NV axis to within a couple degrees [Section 1.4]. We then measure the strength of the magnetic field via the NV $m_s = 0 \rightarrow m_s = -1$ transition frequency, and perform DEER ESR experiments to find the transition frequencies of the electron spins. Plotting the NV transition frequency as well as the central dip of the DEER ESR spectrum and with the B_0 field value shows definitive $g = 2$ character [see Fig. 6.1].

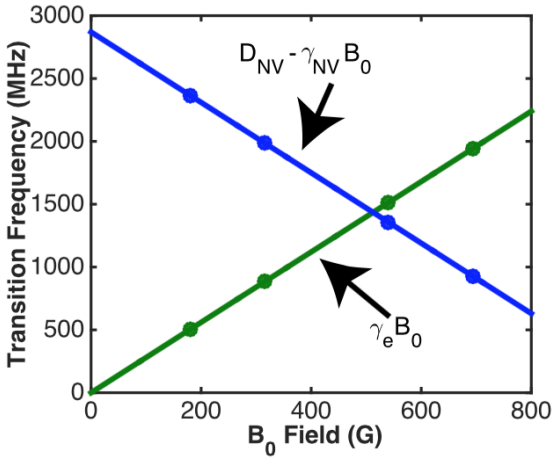

Figure 6.1: NV and electron spin resonance frequencies for various B_0 field values. Blue and green dots are NV ESR and electron spin ESR data, and blue and green lines are theoretical predictions describing the NV transition frequency (neglecting hyperfine and electron spin coupling), and the bare electron spin transition frequency (neglecting NV and electron spin coupling). The NV and electron spin splittings of order 1 MHz are much smaller than the size of the dots.

7 Contrast definition

In order to mitigate noise from laser power drifts over our measurements, we symmeterize every pulse sequence reported in the main text (except for the NV ESR, for which there is no corresponding measurement). For a given sequence that ends in a backprojection on the NV of $\pi/2_\phi$, we repolarize the NV to $m_s = 0$, and repeat the sequence, ending with a pulse of $\pi/2_{\phi+\pi}$ on the NV. For example, a spin echo sequence consists of: $\pi/2_x - \pi_x - \pi/2_x$ [532 nm laser] $\pi/2_x - \pi_x - \pi/2_{-x}$ [532 nm laser] . We read out the signal at each laser pulse. If the amount of photons acquired at the laser pulses are Y_1 and Y_2, respectively, then our contrast is defined to be $(Y_2 - Y_1)/(Y_2 + Y_1)$. This scheme allows us to retain sensitivity while subtracting common-mode noise. In our numerical simulations, shown in Figs. 2(b) and 4(a) in the main text, we allow the contrast to be a free parameter and find the best qualitative fit to the amplitude of the features. Background fluorescence from the buildup of dust on our sample, as well as laser power drifts affecting the optimal readout pulse duration, can change the contrast on our experimental timescales of days. Nonetheless, we find reasonable agreement between the relative size of the measured features and the size of the signals from our numerical simulations.

8 Measurements at misaligned fields

We attempted to recover the dark spin spatial distance information using a technique found in [6], wherein the direction of the bias field (at any magnitude, i.e. away from the ESLAC or GSLAC)

changes the secular dipolar coupling strengths as the NV and dark spin quantization axis become misaligned. The authors found that for a 15° misalignment away from the NV axis, only one frequency appeared in the SEDOR experiment, at around 1 MHz:

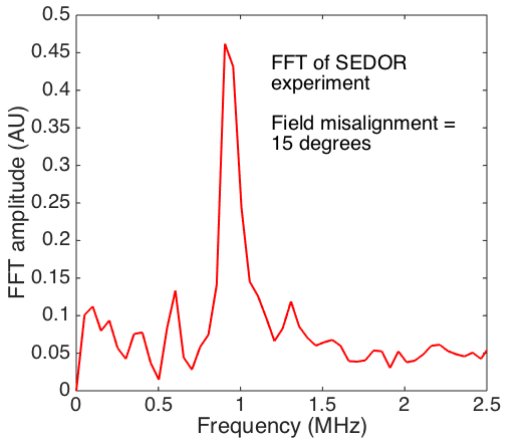

Figure 8.1: FFT of the SEDOR experimental results, under a field misalignment of 15° from the NV axis. Only one frequency appears, implying that the electron spin-spin flip-flops are suppressed.

This observation implies that the NV-dark spin coupling magnitudes remained indistinguishable, and that dark spin flip-flops became suppressed, due to either a reduction in J_{12}, an increase in $\omega_1 - \omega_2$ from g anisotropy, or both. To attempt to recover the electron spin-spin flip-flops at another angle, we repeated the SEDOR experiment, with the misalignment from the NV axis again at 15°, but the azimuthal angle ϕ changed by 7° from the previous measurement. The SEDOR FFT once again shows one peak:

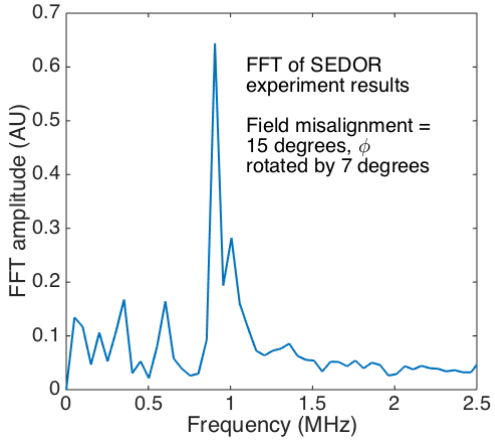

Figure 8.2: FFT of the SEDOR experimental results, under a field misalignment of 15° from the NV axis. Now the azimuthal angle ϕ is changed by 7°. Only one frequency appears, implying that the electron spin-spin flip-flops are suppressed.

The electron spin-spin flip-flops remained suppressed, and the Hamiltonian cannot be uniquely identified. Quantifying this suppression effect, by estimating the g anisotropy and J_{12} at very small misalignment angles, would require field alignment accuracy and precision better than the 2° precision reported here.

References

[1] Arthur Schweiger and Gunnar Jeschke, *Principles of Pulse Electron Paramagnetic Resonance* (Oxford University Press, New York, 2001).

[2] M. D. Calin, and E. Helerea, *Temperature Influence on Magnetic Characteristics of NdFeB Permanent Magnets* (IEEE, Bucharest, Romania, 2011).

[3] B. Green, M. Dale, M. Newton, and D. Fisher, Phys. Rev. B **82**, 165204 (2015).

[4] C. Glover, M. E. Newton, P. Martineau, D. Twitchen, and J. Baker, Phys. Rev. Lett. **90**, 185507 (2003).

[5] O. Tucker, M. Newton and J. Baker, Phys. Rev. B **50**, 15586 (1994).

[6] A. O. Sushkov, I. Lovchinsky, N. Chisholm, R. L. Walsworth, H. Park and M. D. Lukin, Phys. Rev. Lett. **113**, 197601 (2014).